https://dx.doi.org/10.1016/j.jfluidstructs.2016.10.006

Excitation mechanism of rain–wind induced cable vibration in a wind tunnel

Haiquan Jing[1], Yong Xia[1,*], Hui Li[2], Youlin Xu[1], and Yongle Li[3]

[1]*Department of Civil and Environmental Engineering, The Hong Kong Polytechnic University, Hong Kong, China*

[2]*Department of Civil Engineering, Harbin Institute of Technology, Harbin, China*

[3]*Department of Bridge Engineering Southwest Jiaotong University, Chengdu, China*

Abstract

The rain–wind induced vibration (RWIV) of cables in bridge and wind engineering has been reported worldwide over the past decades. However, quantitative analyses of the RWIV mechanism using the real water rivulets are rare. The RWIV of a cable model is tested in an open-jet wind tunnel. The movement and the geometry of the upper rivulet and the vibration of the cable are obtained by videogrammetry. The coupling of the upper rivulet and cable vibration is shown to be the main excitation mechanism of RWIV. In particular, the oscillating upper rivulet induces the boundary layer to attach to the cable and generates aerodynamic forces, which produce a positive work and excite the cable to vibrate. In turn, the cable vibration harmonizes the upper rivulet along the

* Corresponding author. E-mail address: ceyxia@polyu.edu.hk; Tel: +852-27666066.

cable. To verify the proposed mechanism, a numerical model is established using the aerodynamic coefficients measured in dry cable tests. The numerical results are in agreement with the experiments. The effect of the damping ratio on the RWIV amplitude is also experimentally and numerically investigated.

Key words: Cable, Rain−wind induced vibration, Rivulet, Excitation mechanism, Wind tunnel test, Videogrammetry

1 Introduction

Stay cables are prone to large vibrations because of their inherently low damping and great flexibility. These cables are subjected to numerous excitations, including wind, rain, vehicles, and anchorage motion (Xia and Fujino, 2006), or their combinations. Several cables in real bridges exhibit large vibrations under rainy and windy weather conditions. These large cable vibrations are referred to as rain−wind induced vibrations (RWIVs), which are deleterious to stay cables. These vibrations may reduce the fatigue life of the cable and result in connection and protection system failures.

The RWIV of cables has drawn research interest over the past decades. Extensive research has been conducted using field measurements (Main and Jones, 1999; Ni et al., 2007; Zuo et al., 2008, 2010), wind tunnel tests (Hikami and Shiraishi, 1988; Matsumoto et al., 1992, 1995, 2003, 2005; Flamand, 1995; Cosentino et al., 2003a; Gu and Du, 2005; Li et al., 2010a; Li et al., 2015), numerical analyses (Xu and Wang, 2003; Wilde and Witkowski, 2003; Cao et al., 2003; Gu, 2009), and computational fluid dynamics (Lemaitre et al., 2007, 2010; Robertson et al., 2010; Taylor and Robertson, 2011; and Bi et al., 2013, 2014; Wang et al. 2016).

Numerous studies have also been conducted to examine the excitation mechanism of RWIVs. However, researchers have held different or even conflicting ideas and have not established a consensus explanation of this underlying mechanism. Hikami and Shiraishi (1988) first reproduced an RWIV of a cable in a wind tunnel. They demonstrated that the formation of the upper rivulet made the cable unstable and proposed two possible excitation mechanisms: (1) the Den Hartog instability and (2) the instability due to coupled aerodynamic forces. Flamand (1995) verified the essential role of the upper rivulet in RWIV occurrence and also emphasized the importance of the dirt coating of the cable by wind tunnel testing. Cosentino et al. (2003a, b) investigated the movement and thickness of the upper rivulet during a RWIV occurrence and attributed RWIVs to flow regime modification. They reported that the one-bubble regime, which developed at the upper boundary layer during the cable descent, generated a downward aerodynamic force that excited the cable (Cosentino et al., 2003a, b). Seidel and Dinkler (2006) considered the rivulet as a movable disturbance that oscillated around the transition point of the flow at the same frequency as that of the cable vibration. The periodic disturbance induced the periodic transition of the flow from pre-critical to critical flows, resulting in the transfer of energy from the flow to the elastic structure. Matsumoto et al. (1992, 1995, 2003, 2005) conducted a series of wind tunnel tests and classified RWIVs into three types: the galloping type related to a negative slope of the lift force caused by the upper water rivulet or axial flow, the vortex-shedding type with a long period, and the mixed type. They suggested that the three-dimensionality of the Karman vortex shedding and the axial flow are the main excitation sources of the RWIV (Matsumoto et al., 1992, 1995, 2003, 2005).

Gu and Huang (2008) theoretically and experimentally examined RWIVs by treating the upper rivulet as a solid attachment to the cable. They derived an instability criterion for the cable vibration composed of the Den Hartog galloping and the rivulet motion. Xu et al. (2006) measured the aerodynamic coefficients of an inclined cable model with an artificial plastic upper rivulet in a wind tunnel. They observed that the aerodynamic coefficients of the cable varied with the location of the artificial rivulet and concluded that the negative slope of the lift coefficient curve might cause an RWIV (Xu et al., 2006). Du et al. (2013) measured the wind pressure acting on the artificial solid upper rivulet and the inclined cable. They concluded that the significant variation in the aerodynamic forces acting on the cable and the upper rivulet according to the positions of the upper rivulet could cause an RWIV (Du et al., 2013). Xu and Wang (2003), Wilde and Witkowski (2003), and Cao et al. (2003) established numerical models based on the quasi-steady assumption and simulated an RWIV using the cable's aerodynamic coefficients measured in two-dimensional wind tunnel tests. Gu (2009) established a two-dimensional rigid sectional numerical model with a moving upper rivulet on the basis of the quasi-steady assumption and simulated an RWIV using the aerodynamic forces on the inclined cable and the rivulet. In their tests and numerical models, the upper rivulet was assumed to be a solid attachment to the cable surface. This assumption does not match the actual rivulet measured by Cosentino et al. (2003a), Li et al. (2010), Li et al. (2015), and Jing et al. (2015a). The established numerical models might be insufficiently precise to simulate RWIVs because the effects of the variations in the rivulet shape and thickness on the aerodynamic forces and the air–rivulet interaction were not considered.

Although the importance of the upper rivulet in RWIVs has been frequently reported, the precise excitation mechanism of RWIVs remains unclear as information on the rivulet is inadequate. Cosentino et al. (2003a) first measured the position and thickness of the upper rivulet with eight pairs of wires. However, the wires used in the experiment could affect rivulet formation and movement. Li et al. (2010a, b) and Chen et al. (2013) measured the thickness, position, and shape of the upper rivulet by the ultrasonic method. Nevertheless, they only measured the upper rivulet at a fixed section, which might be insufficient to exhibit the rivulet information along the entire cable. Lemaitre et al. (2007, 2010), Robertson et al. (2010), Taylor and Robertson (2011), Bi et al. (2013, 2014), and Cheng et al. (2015) numerically investigated the rivulets on cylinders under the action of wind with the use of the computational fluid dynamic method. However, they simulated the formation and development of the rivulets when the cable was static, and the characteristics of the rivulets in this case may vary from those when the cable vibrates.

Li et al. (2015) and Jing et al. (2015b) proposed videogrammetry to directly measure the rivulet; this noncontact and nonintrusive technique can record all rivulet information, including its movement, shape, and thickness along the entire cable. The present study aims to extend the previous studies by using different types of rivulet simulation. Cable vibration has also been obtained simultaneously. A new excitation mechanism of RWIV is proposed based on the relationship between the cable vibration and the rivulet movement. A numerical model is established to explain how the rivulet exactly excites the cable and how they are strongly coupled together.

2 Wind tunnel tests

The wind tunnel tests were conducted in an open-jet wind tunnel with a rectangular outlet section 1.34 m wide and 1.54 m high. The maximum wind speed of this wind tunnel was approximately 20 m/s. The distribution of the mean wind speed and the turbulence intensity in the outlet section were measured with a cobra probe anemometer point by point at wind speeds (U) of 9.2 and 12.1 m/s, as shown in Figure 1. The variations in the wind speed and turbulence in the outlet section were approximately 3% and 2%, respectively.

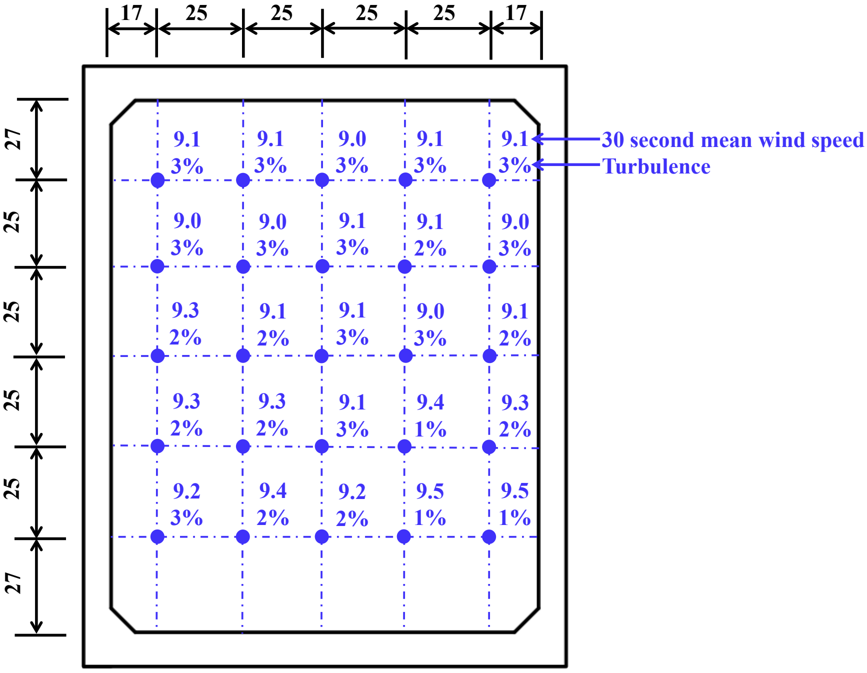

(a) $U = 9.2$ m/s

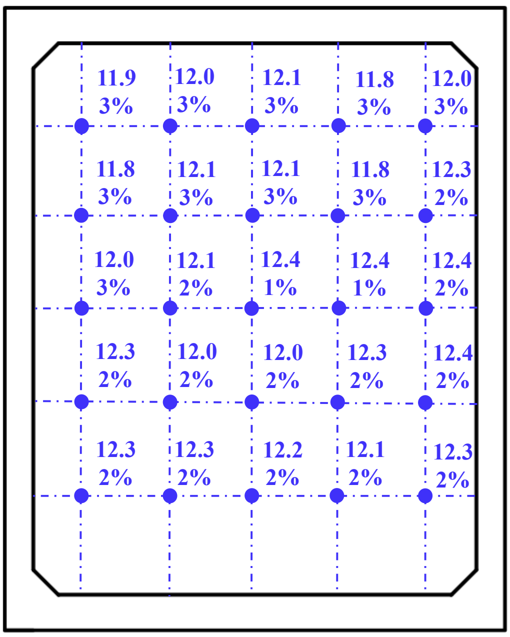

(b) $U = 12.1$ m/s

Figure 1. Wind speed and turbulence distribution in the outlet section of the wind tunnel (length unit: cm; wind speed unit: m/s)

The cable model was suspended about 1 m behind the outlet section as Figure 2 shows. A previous experiment by Li et al. (2007) found that the RWIV was prone to occur when the inclination angle and yaw angle range from 20° to 50° and from 20° to 60°, respectively. In the present study, the inclination angle (α) and yawed angle (β) were set to 32° and 35°, respectively, and the relative yaw angle was calculated as $\beta^* = \sin^{-1}(\sin\beta\cos\alpha) = 29.1°$. Only the in-plane vertical cable vibration was simulated in the present study, as observed by other researchers (Hikami and Shiraishi, 1988; Gu and Du, 2005; Jing et al., 2015a, Li et al. 2015). Four springs suspended the cable in the vertical plane at both ends as Figure 2c shows, and the other end of the springs was mounted on a firm steel frame, which is not shown in this figure. The springs were perpendicular to the cable axis. A steel wire supported the cable in the longitudinal direction. The cable model was 160 mm in diameter and 2.7 m in length with a 2 m-long test segment in the middle and transition segments at both ends. The cable model was made of high-density polyethylene-coated steel tube and elaborated in the same way as real stay cables. The mass of the entire cable model was 66.0 kg. The fundamental frequency was 1.37 Hz, determined using a free vibration test. The cable damping ratio is 0.17%. The corresponding Scruton number was calculated as $S_c = m\zeta/\rho D^2 = 1.70$, where ζ is the damping ratio, ρ is the air density equal to 1.29 kg/m^3, m is the mass of the cable model per unit length, and D is the cable diameter. The Scruton number is close to that of the real stay cables during construction (FHWA, 2007).

(a) Outlet of the wind tunnel

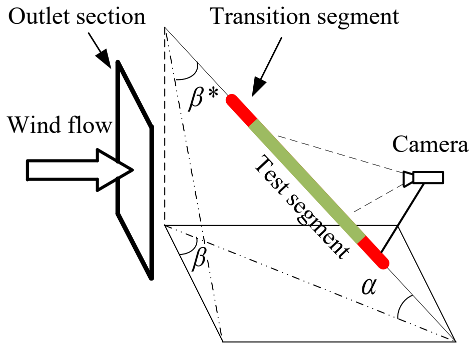

(b) Definition of a yaw angle

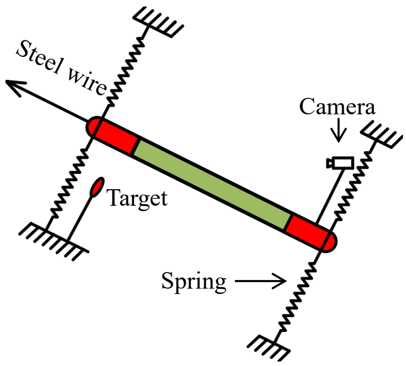

(c) Cable plane

Figure 2. Cable model in a wind tunnel

A digital video camera was mounted on the cable and located 1.2 m above the bottom end of the cable (Figure 2b) such that it has no disturbance on the rivulet and the wake flow. A target with a ruler (Figure 2c) was fixed on the ground. The camera moved with the cable while the target remained steady during the experiment. The camera captured the rivulet, cable, and the target. The movement of the target relative to the camera represents the movement of the camera and the cable. In this manner, the upper rivulet movement and the cable displacement were synchronously measured from the video by videogrammetry (Li et al., 2015; Jing et al., 2015b). By this method, the position of the rivulet along the entire cable could be obtained. The position of the upper rivulet (θ) was measured anticlockwise from the cable top, as shown in Figure 3, which shows only the wind normal to the cable axis (U_N). The angle between the horizontal and wind direction was calculated as $\phi = \arcsin\ (\sin\alpha\sin\beta/\sqrt{\cos^2\beta+\sin^2\alpha\sin^2\beta}) = 20.4^{\circ}$. The localization angle of the upper rivulet from the stagnation point was calculated as $\varphi = \phi + 90^{\circ} - \theta$. The cable displacement (y) was downward positive. The angle between the normal wind and the cable motion was calculated as $\gamma = \phi + 90^{\circ}$.

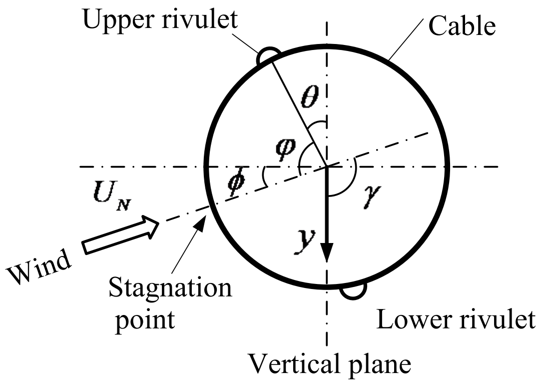

Figure 3. Definition of the rivulet position

3 Simulation of rivulets in wind tunnel tests

Rivulets can be simulated by spraying water (Hikami and Shiraishi, 1988; Matsumoto et al., 1992; Flamand, 1995; Cosentino et al., 2003a; Gu and Du, 2005; Li et al., 2010a), guiding water lines on the cable surface (Mahbub Alam and Zhou, 2007; Li et al., 2015), or their combination (Zhan et al., 2008).

Spraying water simulates an on-site rainfall. The flying raindrops blown by wind gather on the cable surface to form the upper and lower rivulets. Spraying water was widely used in previous wind tunnel studies to reproduce RWIVs (Hikami and Shiraishi, 1988; Matsumoto et al., 1992; Flamand, 1995; Cosentino et al., 2003a; Gu and Du, 2005; Li et al., 2010a), and its effectiveness has been sufficiently verified.

In the guiding water lines technique, small pipes are placed at the upper end of the cable (Jing et al., 2015a, b; Li et al. 2015). The water flows downward along the cable because of gravity and wind pressure, thereby forming the upper and lower rivulets. This simulation approach is also effective and has a significant advantage when applied to wind tunnel tests because there are no raindrops during the test. The flow rate of the rivulet can be well controlled and measured because it depends on the inner diameter of the plastic pipe and the hydraulic head pressure difference. The drawback of this approach is that the surface conditions of the cable are different from those in rainfall, which might affect the movement of the upper rivulet. Improving the wettability of the cable model may be able to eliminate this effect.

On-site rivulets typically contain two parts: the newly gathered rivulets from the raindrops and the formed rivulets flowing down from a higher section. Therefore, the most accurate method for sectional model testing in a wind tunnel is simultaneously spraying water and guiding water lines, as adopted by Zhan et al. (2008).

In the present study, the aforementioned three methods are initially employed under the same wind speed of 12.1 m/s and constant rivulet water flow rate (Q) of 7.46×10^{-7} m^3/s. The wind speed and water flow rate were determined based on previous wind tunnel tests, under which the RWIV was prone to occur. The Reynolds number is derived as $R_e = UD/v = 1.3\times10^5$, where v denotes the kinematic viscosity. In the spraying water method, four nozzles were installed at the top of the wind tunnel outlet section. The rainfall intensity and the flow rate of the upper rivulet were adjusted by controlling the hydraulic pressure of the nozzles. The flow rate of the upper rivulet was measured at the bottom of the cable model using a rain gauge. For the guiding water lines approach, a tank filled with coloured water was placed approximately 0.5 m above the outlet section of the wind tunnel and two plastic pipes were used to guiding the water from the tank to the cable surface. The flow rate was consistent by maintaining the hydraulic head pressure difference unchanged (ignore the cable vibration). The flow rate of the water rivulet was measured at the outlet section of the plastic pipes.

The time history of the cable displacement was measured, as shown in Figure 4. The amplitudes of the simulated cable vibrations obtained using the three methods were 63.6, 74.2, and 73.1 mm, which are very close to each other. The dominant frequencies of the vibrations were the same as the fundamental frequency.

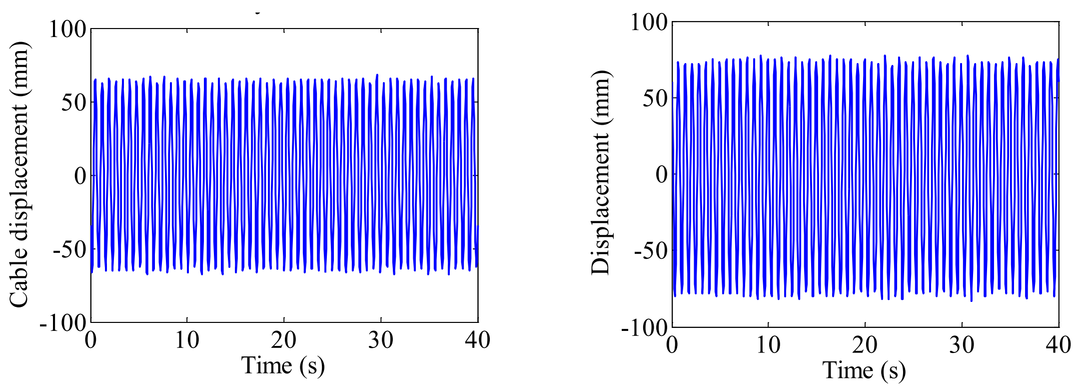

(a) Spraying water only (b) Guiding water lines only

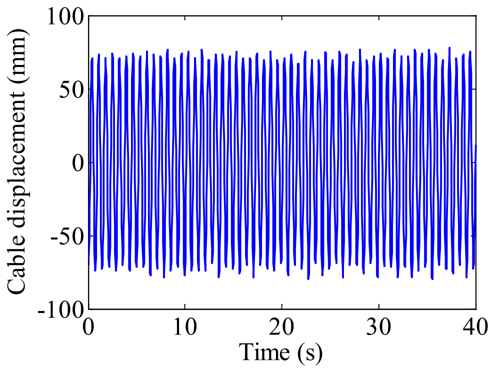

(c) Spraying water and guiding water lines

Figure 4. RWIVs of the cable reproduced by different rivulet simulations

All three rivulet simulations can effectively reproduce RWIV in a wind tunnel. Guiding water lines is adopted hereinafter to investigate the relationship between the upper rivulet and cable vibration because the flying raindrops may damage the measurement instruments.

The identification of the upper rivulet movement has been introduced by Li et al. (2015). The thickness of the upper rivulet was identified based on the relationship between the grayscale intensity and the water thickness (Jing et al., 2015b). As described before, the water used to simulate the rivulet was coloured. Therefore, the rivulet appeared darker in the grayscale image, in particular, the thicker it was, the darker it became. Besides, the water thickness was assumed to be proportional to the grayscale intensity. The scaling factor was calibrated using the water flow rate of the upper rivulet. Consequently, the thickness of the rivulet was identified from the grayscale intensity of the rivulet in the grayscale image.

4 Characteristics of the rivulets in RWIV

When the cable vibrated with an amplitude of 74.2 mm, which corresponds to the non-dimensional amplitude of 0.46 (= 74.2/160.0) at the fundamental frequency of 1.37 Hz, the upper rivulet position is identified as shown in the video (can be downloaded from the online supplementary material). The rivulet position slightly varied along the cable; thus, the averaged position is shown in Figure 5. The averaged upper rivulet oscillated between 6.6° and 33.0°, with an equilibrium position of 18.9°. The vibration frequency of the averaged upper rivulet was the same as the fundamental frequency of the cable. Figure 6 compares the averaged upper rivulet position and the cable displacement. As shown in Figure 6, the upper rivulet oscillated almost in-phase with the cable. When the cable moved upward (the displacement becomes smaller in the figure), the upper rivulet moved to leeward (the angle becomes smaller). Conversely, when the cable moved downward, the rivulet moved upwind. Coesentino et al. (2003a) also observed this phenomenon, in which the mean position of the upper rivulet oscillated between 13° and 25°.

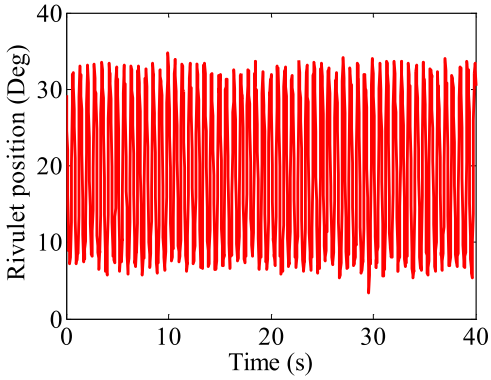

Figure 5. Time history of the upper rivulet

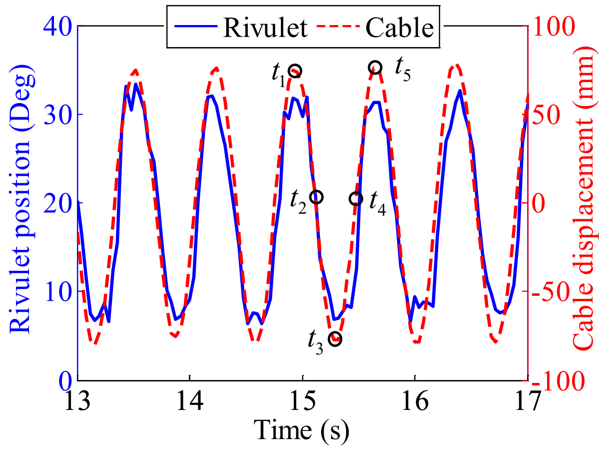

Figure 6. Comparison of the upper rivulet and cable oscillation

Compared with the upper rivulet, the lower rivulet was observed to be stable by the experimenter during the test. Its thickness, position, and shape were almost constant. The results of the lower rivulet are not shown here.

Images of the upper rivulets during one cycle (t_1 to t_5) were captured to discover the relation between the upper rivulet and the cable vibration. These images are shown in Figure 7.

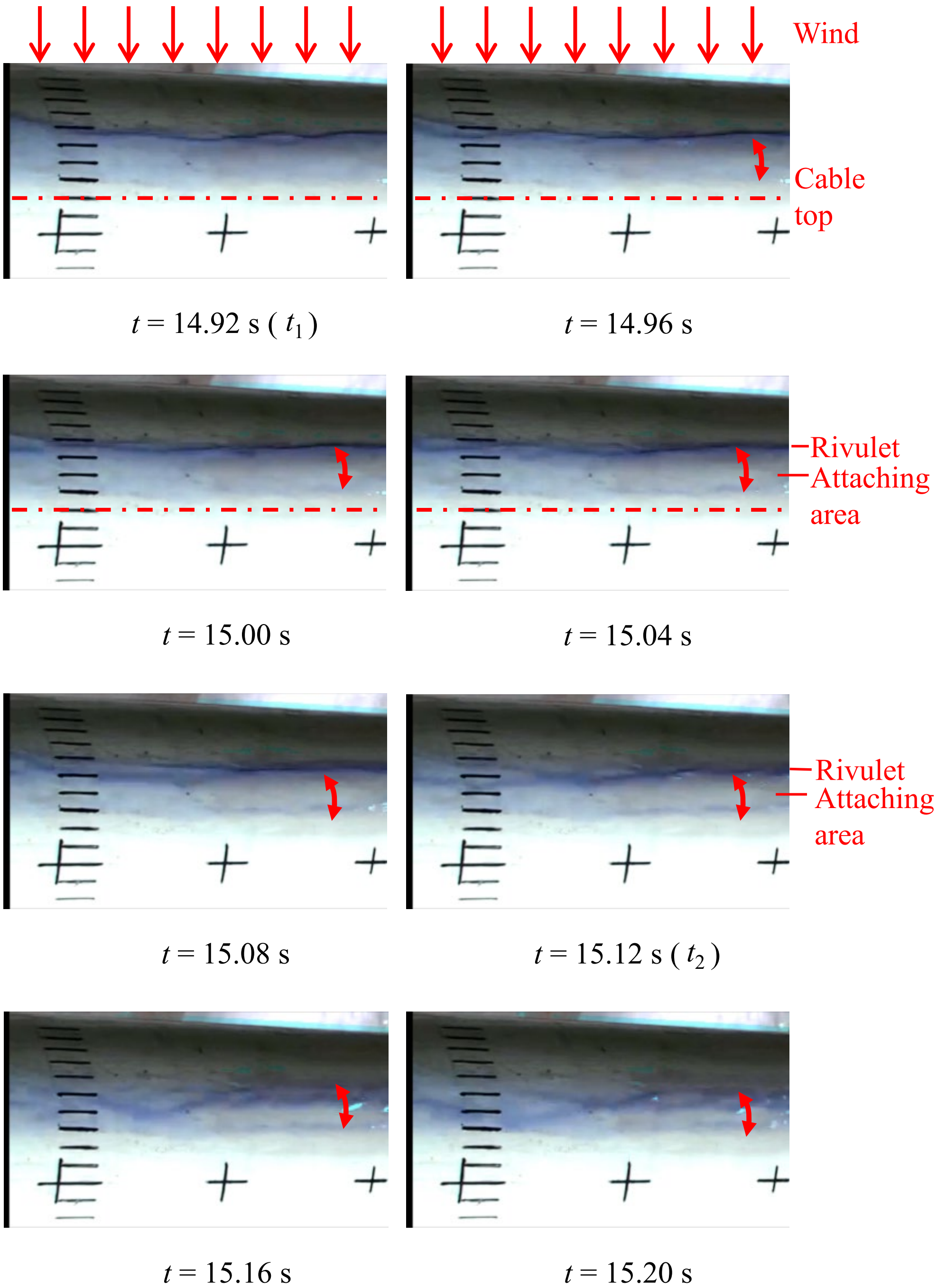

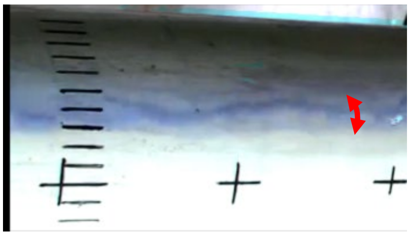

$t = 15.24$ s

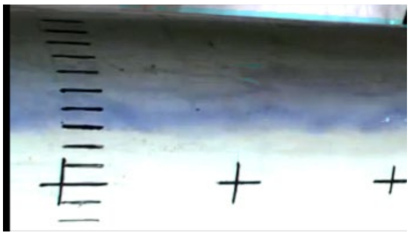

$t = 15.28$ s (t_3)

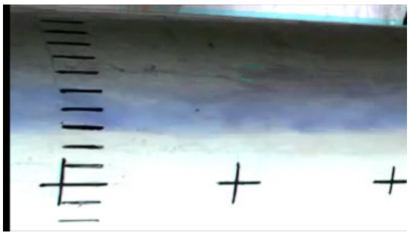

$t = 15.32$ s

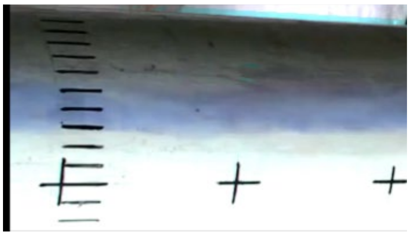

$t = 15.36$ s

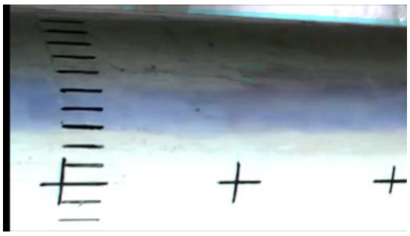

$t = 15.40$ s

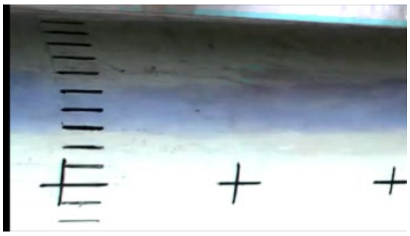

$t = 15.44$ s

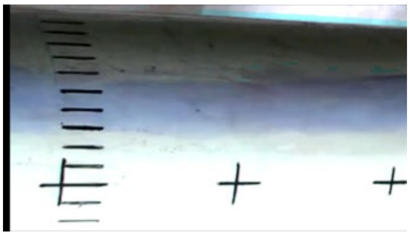

$t = 15.48$ s (t_4)

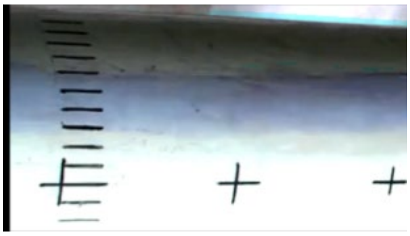

$t = 15.52$ s

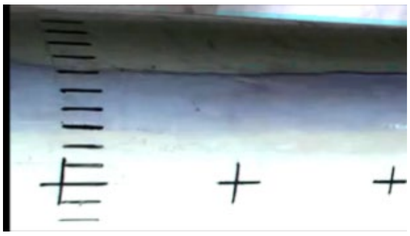

$t = 15.56$ s

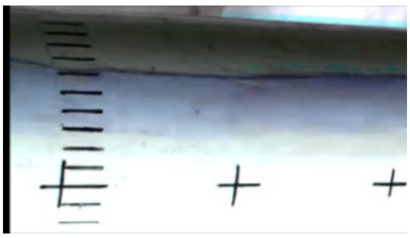

$t = 15.60$ s

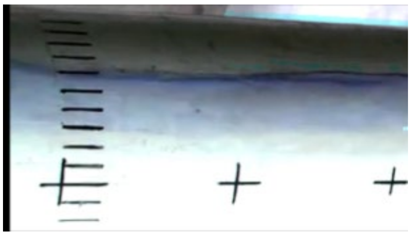

t = 15.64 s (t_5)

Figure 7. Captured images of the upper rivulet from t_1 to t_5 (denotes the attaching area)

At t_1 (t = 14.92 s), the cable was located at the lowest position, and the upper rivulet was located away from the cable top. The upper rivulet was hump-shaped with a carpet behind and coherent along the cable axis. The cable then moved upward from the lowest position. The upper rivulet moved to leeward from 14.92 to 15.12 s (t_1 to t_2) and maintained the hump shape and coherence. However, the carpet behind the rivulet was pressed and forced to gather in leeward, forming another smaller hump-like shape far behind the rivulet, as shown clearly at t = 15.12 s. After the cable and upper rivulet passed their equilibrium position around t_2 (15.12 s), the upper rivulet began to flatten and the distribution along the cable axis became less coherent as shown at t = 15.20 s. In addition, the weakening colour intensity indicates that the water thickness decreased during this process, as measured by Jing et al. (2015b). When the cable reached the highest position at t_3 (t = 15.28 s), the rainwater totally spread out, resembling a water carpet with wide and flat geometry. The rainwater was coherently distributed along the cable axis. The surface of the upper rivulet became very smooth and almost stuck on the cable surface.

When the cable moved downward, the upper rivulet slid back upwind as a water carpet. From t_3 to t_4, the upper rivulet maintained its flat shape and smooth surface such that its location and movement were almost indistinguishable in the figure (the video provides better contrast and the rivulet is recognizable). After the cable and the upper rivulet crossed their equilibrium position (from t_4 to t_5), the upper rivulet began to gather and rose to the most upwind position. When the cable reached the lowest position at t_5 (t = 15.64 s), the thickest upper rivulet, as that at t_1, was observed.

Figure 7 shows that the geometry of the upper rivulet is strongly related to the cable vibration. During a one-cycle cable vibration, the upper rivulet varied not only in position but also in thickness, distribution, and shape. The observed in-phase vibrations of the upper rivulet and the cable are consistent with the previous measurement obtained by Cosentino et al. (2003a) and Jing et al. (2015b). However, the thickness of the upper rivulet in the present study is different from that obtained by Cosentino et al. (2003a). In their test, the upper rivulet was clearly marked during the cable descent and spread out when it reached the lowest position, the rivulet became disorganized when the cable moved upward, and the thickest rivulet was observed when the cable was close to the equilibrium position during descent (Cosentino et al., 2003a). The difference of the two studies might be caused by the disturbance of the experimental instruments on the rivulet in their study.

5 Excitation mechanism of RWIV

From the observed rivulet and cable vibration, a new excitation mechanism of RWIV is proposed in this study on the basis of the flow passing a dry inclined circular cylinder (Flamand and Boujard, 2009; Nikitas et al., 2012; Jakobsen et al., 2012; Benidir et al., 2015).

5.1 Experimental observations

Figure 7 confirms that the upper rivulet is composed of a circumferentially oscillating water carpet on which a hump evolves under the action of local wind pressure during the cable vibration, as described by Lemaitre et al. (2010). As the cable moved upward (t_1 to t_3), the water accumulated to a hump shaped rivulet and the carpet behind the rivulet was pressed to gather in leeward. The hump−shaped rivulet then spread to a flat water carpet when the cable reached the highest position. As the cable moved downward (t_3 to t_5), the flat water carpet flowed down and then gathered to form a hump−shaped rivulet when the cable reached the lowest position. During this process, the separation state of the boundary layer was deduced from the shape of the upper rivulet, similar to the oil visualization (Kleissl and Georgakis, 2012).

Based on the observed upper rivulet information, the possible wind flow field at different instants is deduced and sketched in Figure 8, in a similar way as Panton (2013) and Devenport and Borgoltz (2016) did. In this figure, the upper rivulet is exaggerated for enhanced visibility, and the lower rivulet is removed because it has little effect on the RWIV. At t_1 or t_5, the cable was located at the lowest position, the upper rivulet accumulated to a hump with a water carpet behind, and the boundary layer should separate at the original separation point, as shown in Figure 8a. The water carpet behind the upper rivulet was relatively thick because it was located at the leeward of the separation point and no significant wind pressure acted on its surface. When the cable moved upward (t_1 to t_3), the attacking angle moved clockwise (see Figure 8b), the boundary layer attached to the rivulet, the wind flowed along its surface, and then separated at a position far behind the original separation point. As a result, the wind pressure on the water carpet surface changed and the water carpet behind the rivulet attenuated and was pushed to leeward (Figure 8b). When the cable moved downward (t_3 to t_5), the attacking angle moved anti-clockwise (see Figure 8d), and the boundary layer did not attach but turned to separate at the original separation point (Figures 8c, 8d). The water rivulet was located at the leeward of the separation point and there was no significant wind pressure acting on its surface. Consequently, the water rivulet turned to a flat water carpet flowing down from the cable top.

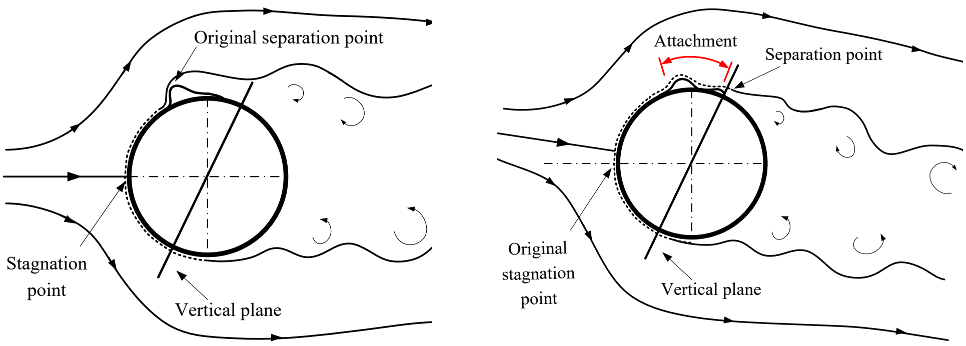

(a) t_1 or t_5 (b) t_2

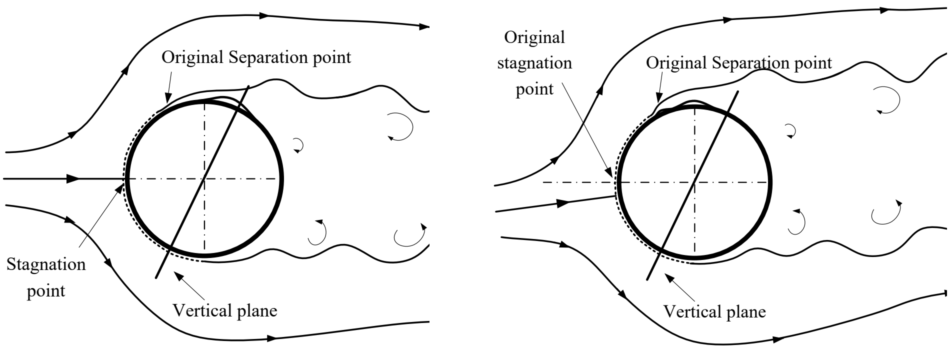

(c) t_3 (d) t_4

Figure 8. Sketch of the flow passing the cable

The boundary layer attachment significantly affects the wind pressure distributions around the cable (Zdravkovich, 1997). After the transition occurred in the boundary layer, the flow state can be categorized into five flow regimes (Zdravkovich, 1997): pre-critical regime [(100k–200k) < R_e < (300k–340k)]; one-bubble regime [(300k–340k) < R_e < (380k–400k)]; two-bubble regime [(380k–400k) < R_e < (500k–1M)]; super-critical regime [(500k–1) < R_e < (3.5M–6M)]; post-critical regime [(3.5M–6M) < R_e]. In the one-bubble regime, the boundary layer reattaches to only one side of the cylinder. This asymmetric reattachment of the boundary layer forms a separation bubble on one side of the cylinder and produces a much lower pressure on this side than on the opposite side (Figure 9), thereby generating a large lift force. When the wind is normal to the circular cylinder, the reattachment stochastically occurs on either side in this regime (Zdravkovich, 1997). Recently, Larose et al. (2003), Flamand and Boujard (2009), Nikitas et al. (2012), Jakobsen et al. (2012), Nikitas and Macdonald (2015), and Benidir et al. (2015) measured the wind pressure around an inclined dry cable in the critical Reynolds number regime. They observed the asymmetric pressure distribution and a sudden increase in the lift coefficient in the one-bubble regime and tried to explain the dry cable galloping using these properties. They observed that the sudden increase in the lift coefficient was caused by the asymmetric boundary layer attachment.

Different from the wind normal to the cable case, for the inclined and yaw cable, asymmetric reattachment always occurs on the same side (Flamand and Boujard, 2009) because the boundary layer is highly sensitive to disturbances, surface roughness, and turbulent free stream.

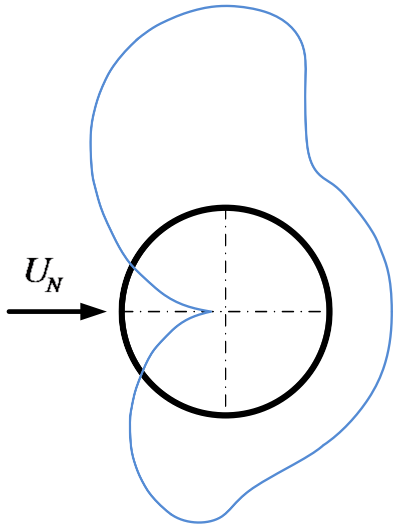

Figure 9. Wind pressure distribution in the one-bubble regime (Zdravkovich, 1997; Jakobsen et al., 2012; Benidir et al., 2015): a reattachment occurring on the upper side

Given the above properties of asymmetric flow attachment to the dry inclined cylinder, the asymmetric boundary layer attachment in the present RWIV should also lead to an asymmetric wind pressure and a significant lift force on the cable when the cable moved upward. This attachment was induced by the upper rivulet because the Reynolds number of the present cable (1.3×10^5) was in the pre-critical regime and was lower than that in the one-bubble regime. However, the pressure distribution induced by the asymmetric attachment should be similar as shown in Figure 9 and Figure 10a. Consequently, the excitation mechanism of RWIV can be briefly explained as follows. When the cable moved upward, the aerodynamic forces were upward and produced a positive work to excite the cable. After the cable reached the highest and started to move downward, the upper rivulet spread out and became a water carpet. The boundary layer attachment disappeared and separated at the original separation point. The corresponding pressure distribution became symmetric around the cable, as shown in Figure 10b. The aerodynamic forces produce a negative work as in the pre-critical regime.

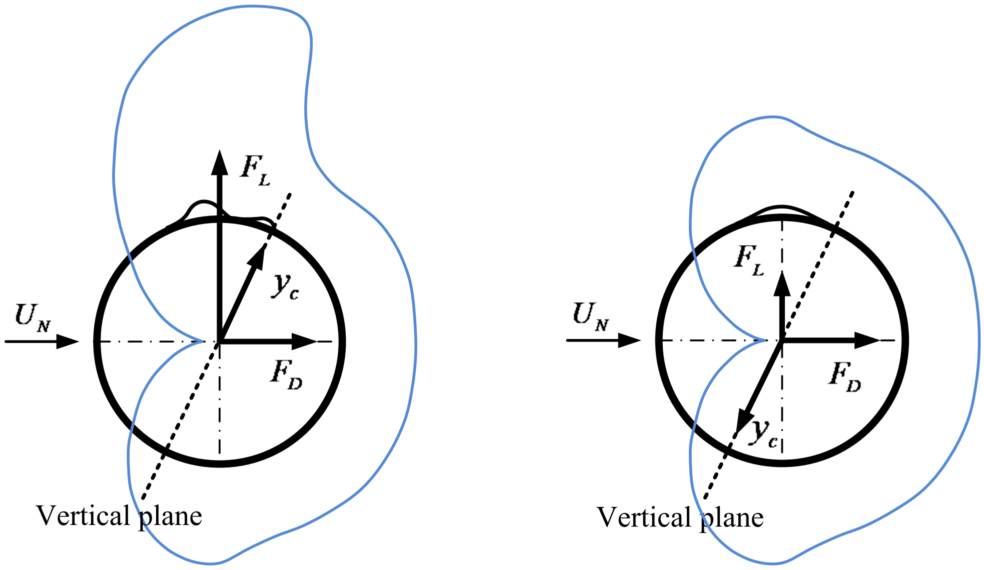

(a) Cable moves upward (b) Cable moves downward

Figure 10. Sketch of pressure distribution on the cable (F_D: drag force; F_L: lift force; y_c: cable displacement)

Similar expressions were proposed by Cosentino et al. (2003a, b) and Seidel and Dinkler (2006). Cosentino et al. (2003a, b) treated the upper rivulet as an obstacle close to the upper boundary layer separation point and modified the flow state from the pre-critical regime to the critical regime. They observed that the rainwater that spread gathered at the cable top when the cable moved downward and assumed that the gathered upper rivulet modified the flow regime into the one-bubble regime, which generated a downward lift force and produced a positive aerodynamic work to excite the cable vibration. However, in the present experiment, the upper rivulet mainly gathered in a position away from the cable top when the cable was located at the lowest position. In addition, the reattachment of the boundary layer to the top side produces upward aerodynamic forces rather than downward forces, thereby generating a negative work if the cable was descending. Seidel and Dinkler (2006) considered upper and lower rivulets as movable disturbances and assumed that, when a rivulet is located at the separation area, the flow transits from the pre-critical regime to the critical regime, as what happens in the Prandtl trip wire phenomenon. However, in their study, the effects of the rivulets when the cable moved upward and downward were not differentiated.

5.2 Difference between the upper and lower rivulets

In this study, only the upper rivulet is considered, whereas the lower rivulet is disregarded. The lower rivulet cannot induce the boundary layer to attach on the cable because it is too thick or located at the leeward of the separation point. Even though both the upper and lower rivulets were reported to be symmetrically located on the cable surface with respect to the stagnation point by Gu and Du (2005) and Lemaitre et al. (2007, 2010), they exhibit different states when the cable is static because of the different gravitational effects. As shown in Figure 11a, the upper rivulet is subjected to gravity g, wind pressure P, and reaction of the cable S. In the same figure, γ_u and γ_d

denote the upstream and downstream contact angle, respectively. Gravity tends to keep the upper rivulet on the cable surface and subjects the water under compression in the vertical direction. Therefore, the upper rivulet is prone to becoming relatively thin and flat as well as deformed under external loads. When the cable is vibrating, the upper rivulet may change its shape and position to induce and respond to the boundary layer attachment. The upper rivulet can move forth and back on the cable surface in a non-stationary manner even though the cable is static.

As for the lower rivulet (Figure 11b), gravity tends to pull the rainwater away from the cable and causes the water under tension in the vertical direction, making the lower rivulet close to the bottom of the cable and thicker than the upper one. As a result, the lower rivulet might be too thick to induce the boundary layer attachment or located at the leeward of the separation point. Therefore, the lower rivulet exerts minimal effect on RWIV, and no significantly variant tangential wind force is present to excite the lower rivulet when the cable is static or vibrating. In addition, gravity maintains the contact angles smaller than the critical angle, enhancing the stability of the lower rivulet.

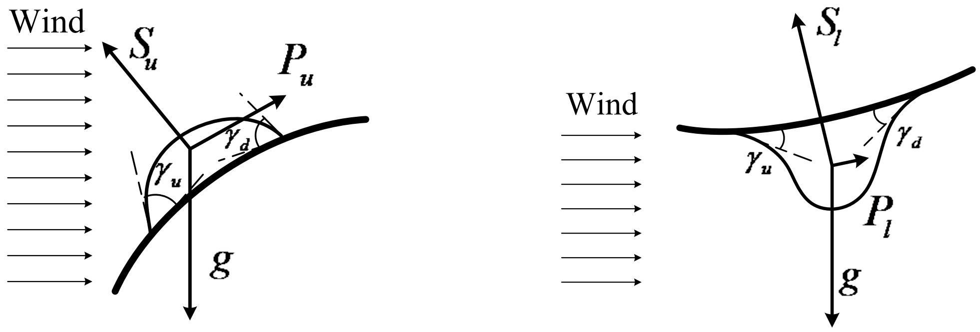

(a) Upper rivulet (b) Lower rivulet

Figure 11. Forces on the upper and lower rivulets

5.3 Numerical analysis

The explanations in Sections 5.1 and 5.2 are verified using the numerical analysis in this section. An inclined cable subjected to yaw wind flow, as shown in Figure 2b, is considered. The angle of the wind velocity relative to the cable axis is defined as the cable-wind angle (Φ) (Figure 12), which is calculated as 90° − β^* (Macdonald and Larose, 2006). The cable is assumed to move at a velocity of $\dot{y}$ in the vertical plane and normal to its axis. The angle between the cable velocity and the cable-wind plane is γ as Figure 13 shows. The magnitude of the relative incident velocity considering the cable velocity is

$$U_R = \sqrt{(U_R^1)^2 + (U_R^2)^2} = \sqrt{U^2 - 2U\dot{y}\sin\Phi\cos\gamma + \dot{y}^2} \tag{1}$$

where U_R^1 is the projection of U_R in the cable-wind plane (Figure 12b), and U_R^2 is the projection of U_R normal to the cable-wind plane, as Figure 13 shows.

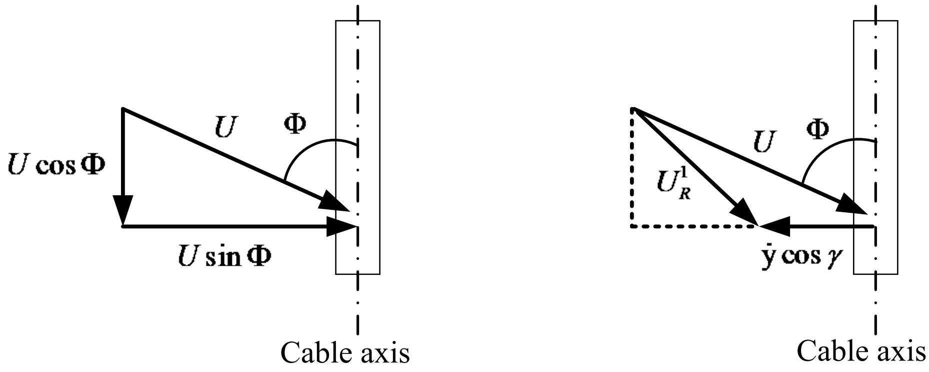

(a) Absolute velocities (b) Velocity relative to cable

Figure 12. Velocities in the cable-wind plane

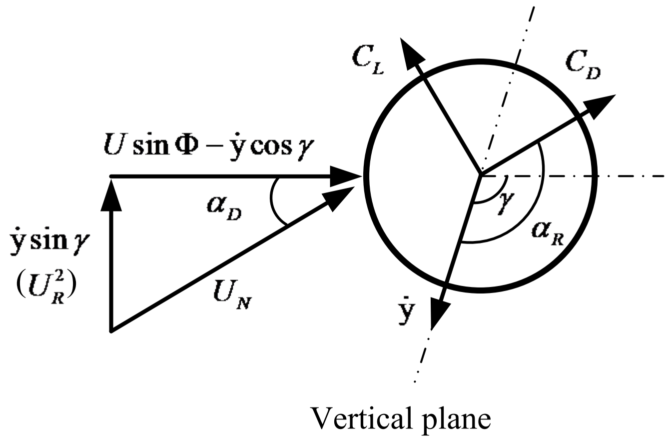

Figure 13. Velocities and forces in the plane normal to the cable axis

Consequently, the attacking angle (α_D) induced by the cable velocity (see Figure 13) is given by

$$\alpha_D=\text{atan}\,[\,\dot{y}\sin\gamma/(U\sin\Phi-\dot{y}\cos\gamma)] \tag{2}$$

The relative velocity induces drag and lift forces, given by equation (3), per unit length of the cylinder normal to its axis.

$$\begin{cases} F_D = \frac{1}{2}\rho U_R^2 D C_D \\ F_L = \frac{1}{2}\rho U_R^2 D C_L \end{cases}, \tag{3}$$

where C_D and C_L are the drag and lift coefficients, respectively.

The angle between the drag force and the cable motion in Figure 13 is given by

$$\alpha_R = \gamma + \alpha_D. \tag{4}$$

Thus, the aerodynamic force per unit length in the cable vibration direction is

$$F_a = \frac{1}{2}\rho U_R^2 D[C_D \cos\alpha_R - C_L \sin\alpha_R]. \tag{5}$$

During a cycle, the aerodynamic work attributed to the aerodynamic force can be calculated as

$$E_a = \int_0^T F_a \dot{y} dt, \tag{6}$$

where T is the period of the cable vibration.

Substituting equation (5) into equation (6) and separating the lift and drag components, one has

$$E_a = E_L + E_D, \tag{7}$$

where $E_L = -\frac{1}{2}\int_0^T \rho U_R^2 D C_L \sin\alpha_R \dot{y} dt$ and $E_D = \frac{1}{2}\int_0^T \rho U_R^2 D C_D \cos\alpha_R \dot{y} dt$ represent the work by the lift and drag forces, respectively.

In the wind tunnel tests, the cable is designed to be a linear single-degree-of-freedom vibration system. Only the structural damping consumes energy, which can be calculated as

$$E_s = -\int_0^T 2m\omega\zeta\dot{y}^2 dt \tag{8}$$

The stability of the cable can be evaluated by the total work during a cycle.

$$E = E_a + E_s \tag{9}$$

Depending on the value of the total work E, the cable vibration can be (1) stable ($E = 0$), (2) increasing ($E > 0$), or (3) decaying ($E < 0$).

The cable exhibits a harmonic vibration when the vibration reaches a steady state. Therefore, the velocity time history is written as

$$\dot{y} = A\omega \sin\omega t \tag{10}$$

where A is the displacement amplitude and ω is the circular frequency.

On the basis of the proposed excitation mechanism, the aerodynamic forces are closely related to the boundary layer attachment or the rivulet movement, which interacts with the cable vibration. Thus, the aerodynamic force coefficients are assumed to be associated with the cable vibration. It is also assumed that when the upper rivulet induces the boundary layer attachment, the aerodynamic forces of the cable with the rivulet are similar to those in the one-bubble regime, while when the upper rivulet does not induce the boundary layer attachment, the aerodynamic forces of the cable are similar to those in the pre-critical regime. Take the measurement data by Jakobsen et al. (2012) as a reference. They measured the wind pressure of an inclined cable with a geometry of D = 160 mm and Φ = 60°, which is almost the same as the cable in the present study. When the cable moved downward, the rivulet exerted almost no effect on the wind pressure distribution, indicating that the drag and lift coefficients were the same as those of the dry cable in the pre-critical regime. They obtained the following coefficients when U = 11.34 m/s (R_e= 1.2×10^5, close to the present study): $C_D = 0.79$ and $C_L = 0$. However, when the cable moved upward, the rivulet induced the flow attached to the cable asymmetrically; this flow generated a wind pressure similar to that in the one-bubble regime. During the process, the drag and lift coefficients were 0.51 and 0.58, respectively, at a wind speed of 20.2 m/s in the one-bubble regime (R_e= 2.14×10^5, much higher than the present study). Figure 8 shows that the rivulet-induced attachment was not steady. When the cylinder exhibited the strongest upward velocity, the attachment had the strongest intensity. By contrast, when the cylinder speed was considerably decreased, the attachment intensity weakened. Therefore, we assume that the drag and lift coefficients exhibit a linear relationship with the cable vibration speed. Consequently, the following equation is used:

$$C_L=\begin{cases} C_U(0.51\dot{y}/\omega A) & (\dot{y}<0) \\ 0 & (\dot{y}\geq 0) \end{cases} \quad C_D=\begin{cases} 0.79+C_U(0.79-0.58)\dot{y}/\omega A & (\dot{y}<0) \\ 0.79 & (\dot{y}\geq 0) \end{cases} \tag{11}$$

where $0 \leq C_U \leq 1$ is the uniform coefficient and denotes the coherence of the boundary layer attachment along the cable. When the attachment is ideally uniform along the cable, C_U is equal to 1; when the attachment is completely chaotic along the cable, C_U is equal to 0. It is worth to note that Equation (11) is a linear interpolation of the aerodynamic force coefficients. Although be accurate, it provides a simplified approach to the initial model development. More accurate models need further investigations.

The relationship between the aerodynamic work and the cable vibration amplitude is obtained by substituting equations (10) and (11) into equation (9) and applying numerical integration. Two cases, namely, ideally uniform (C_U = 1.0) and nonuniform (C_U =0.7), are analyzed, and the results are shown in Figure 14. In the figure, the cable vibration amplitude is normalized by dividing the cable diameter. Figure 14 also shows that both structural damping and drag force exerts a negative work on the system, whereas the lift force exerts a positive work. The total input energy (E) initially increases and subsequently decreases with an increase in the nondimensional amplitude.

When E equals zero, the nondimensional amplitude is defined as the critical amplitude (C_A), indicating that the cable could steadily vibrate at this amplitude. For the ideally uniform case (C_U = 1.0), C_A is 1.59, which is much larger than the present observation (0.46) in the wind tunnel test. When the nonuniform rivulet is considered (C_U = 0.7), C_A is 1.03. The cable amplitude decreases when the boundary layer attachment is nonuniform (Jing et al., 2015a). The difference between the experimental observations and the numerical results could be attributed to the nonlinearity of the springs damping under large deformation (Cosentino et al., 2003a) and the aerodynamic coefficients. Nevertheless, this numerical analysis qualitatively verifies the proposed cable vibration mechanism.

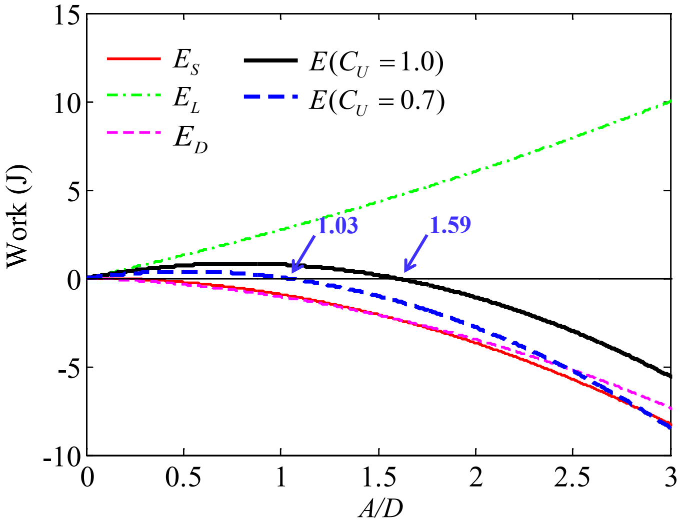

Figure 14. Work versus nondimensional cable vibration amplitude

Consequently, the excitation mechanism of RWIV is summarized as the interaction between the cable, the boundary layer, and the upper rivulet as Figure 15 shows. When the cable moves upward, the formation and oscillation of the upper rivulet induces the boundary layer to attach to the cable, changes the wind pressure distribution, and generates distinct upward lift forces and lower drag forces, as what happens in the one-bubble regime. The aerodynamic forces acting on the cable produce a positive aerodynamic work and excite the cable vibration. The local wind pressure changes the upper rivulet's shape. The cable vibration, in turn, changes the attacking angle of the wind and provides inertial force on the upper rivulet, exciting the upper rivulet to steadily and circumferentially oscillate on the cable surface. Consequently, the steadily and circumferentially oscillating upper rivulet induces the boundary layer to attach. Besides, the cable vibration also enhances the coherence of the upper rivulet along the cable and harmonizes the attachment of the boundary layer along the cable, resulting in larger resultant forces on the cable. When the interaction between the cable, upper rivulet, and boundary layer reaches a stationary equilibrium state, the RWIV of the cable reaches a steady state. However, as reported in a previous study (Jing et al., 2015a), the stationary equilibrium state of this system could be non-unique and multiple in accordance with the different initial conditions of the cable and the rivulet.

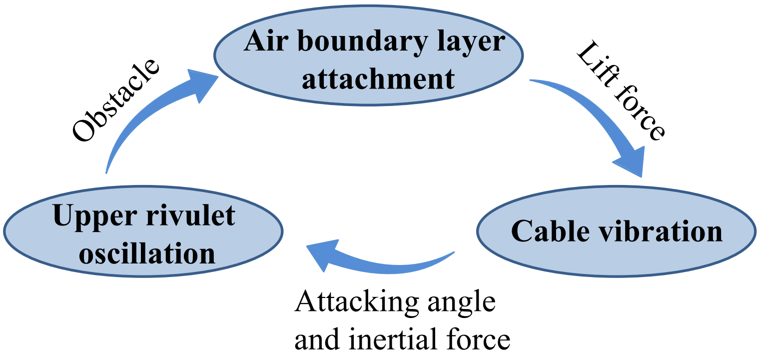

Figure 15. Interaction between the upper rivulet, boundary layer, and the cable

6 Conclusions

In this study, the RWIV of a stay cable is successfully reproduced in an open-jet wind tunnel. The upper rivulet and the cable displacement are synchronously measured by videogrammetry. From the observed upper rivulet characteristics and the cable vibration, a new excitation mechanism of RWIV is proposed, and a verification numerical model is established. The main conclusions are as follows:

(1) When a large RWIV of a cable occurs, the upper rivulet circumferentially oscillates on the cable surface. The oscillation is relatively coherent along the entire cable and almost in-phase with the cable when the vibration amplitude is relatively large.

(2) The excitation of the RWIV can be attributed to the interaction between the cable, boundary layer, and upper rivulet. When the cable moves upward, the

oscillating upper rivulet induce the boundary layer to attach to the top side of the cable, generating upward aerodynamic forces that exert a positive work on the system. The cable vibration, in turn, harmonizes the upper rivulet oscillation through relative wind direction variation and inertial force.

(3) The established numerical model qualitatively has verified the proposed excitation mechanism.

Acknowledgment

The study was supported by the Research Grants Council of Hong Kong (No. PolyU 5298/11E). The experiment was conducted at Southwest Jiaotong University, China. The assistance provided by Dr. Huoyue Xiang and Mr. Chao Sun from Southwest Jiaotong University is greatly appreciated.

References

Bi, J.H., Lu, P., Wang, J., Bao, C., Guan, J., 2014. Numerical simulation and analysis of the effects of water-film morphological changes on the aerodynamic lift of stay cables. Journal of Fluids and Structures 48, 376–392.

Bi, J.H., Wang, J., Shao, Q., Lu, P., Guan, J., Li, Q.B., 2013. 2D numerical analysis on evolution of water film and cable vibration response subject to wind and rain. Journal of Wind Engineering and Industrial Aerodynamics 121, 49–59.

Benidir, A., Flamand, O., Gaillet, L., Dimitriadis, G., 2015. Impact of roughness and circularity-defect on bridge cables stability. Journal of Wind Engineering and Industrial Aerodynamics 137, 1–13.

Cao, D.Q., Tucker, R.W., Wang, C., 2003. A stochastic approach to cable dynamics with moving rivulets. Journal of Sound and Vibration 268, 291–304.

Chen, W.L., Tang, S.R., Li, H., Hu, H., 2013. Influence of dynamic properties and position of rivulet on rain–wind-induced vibration of stay cables. Journal of Bridge Engineering 18, 1021–1031.

Cheng, P., Li, H., Fuster, D., Chen, W.L., Zaleski, S., 2015. Multi-scale simulation of rainwater morphology evolution on a cylinder subjected to wind. Computers & Fluids 123, 112–121.

Cosentino, N., Flamand, O., Ceccoli, C., 2003a. Rain–wind induced vibration of inclined stay cables, Part I: experimental investigation and physical explanation. Wind and Structures 6, 471–484.

Cosentino, N., Flamand, O., Ceccoli, C., 2003b. Rain–wind induced vibration of inclined stay cables. Part II: Mechanical modeling and parameter characterization. Wind and Structure 6, 485-498.

Devenport, W.J., Borgoltz, A., 2016. Flow Past a Circular Cylinder, Virginia Tech University, Available: http://www.dept.aoe.vt.edu/~aborgolt/aoe3054/manual/expt3/index.html.

Du, X.Q., Gu, M., Chen, S.R., 2013. Aerodynamic characteristics of an inclined and yawed circular cylinder with artificial rivulet. Journal of Fluids and Structures 43, 64–82.

FHWA, 2007. Wind-Induced Vibration of Stay Cables, Report of Federal Highway Administration, FHWA-HRT-05-083.

Flamand, O., 1995. Rain–wind induced vibration of cables. Journal of Wind Engineering and Industrial Aerodynamics 57, 353–362.

Flamand, O., Boujard, O. 2009. A comparison between dry cylinder galloping and rain–wind induced excitation. 5th European & African Conference on Wind Engineering, Florence, Italy.

Gu, M., 2009. On wind–rain induced vibration of cables of cable-stayed bridges based on quasi-steady assumption, Journal of Wind Engineering and Industrial Aerodynamics 97, 381–391.

Gu, M., Du, X.Q., 2005. Experimental investigation of rain–wind induced vibration of cables in cable-stayed bridges and its mitigation. Journal of Wind Engineering and Industrial Aerodynamics 93, 79–95.

Gu, M., Huang, L., 2008. Theoretical and experimental studies on the aerodynamic instability of a two-dimensional circular cylinder with a moving attachment. Journal of Fluids and Structures 24, 200–211.

Hikami, Y., Shiraishi, N., 1988. Rain–wind induced vibrations of cables stayed bridges. Journal of Wind Engineering and Industrial Aerodynamics 29, 408–418.

Jakobsen, J.B., Andersen, T.L., Macdonald, J.H.G., Nikitas, N., Larose, G.L., Savage, M.G., McAuliffe, B.R., 2012. Wind-induced response and excitation characteristics of an inclined cable model in the critical Reynolds number range. Journal of Wind Engineering and Industrial Aerodynamics 110, 100–112.

Jing, H.Q., Xia, Y., Li, H., Xu, Y.L., Li, Y.L., 2015a. Study on the role of rivulets in rain–wind induced cable vibration through wind tunnel testing. Journal of Fluids and Structures 59, 316–327.

Jing, H.Q., Xia, Y., Xu, Y.L., Li, Y.L., 2015b. Measurement of rivulets' movement and thickness on inclined cable through digital image processing. Smart Structures and Systems. Accepted.

Kleissl, K., Georgakis, C.T., 2012. Comparison of the aerodynamics of bridge cables with helical fillets and a pattern-indented surface. Journal of Wind Engineering and Industrial Aerodynamics 104–106, 166–175.

Larose, G.L., Savage, M.G., Jakobsen, J.B., 2003. Wind tunnel experiments on an inclined and yawed circular cylinder in the critical Reynolds number range. Proceedings of 11th International Conference on Wind Engineering, Lubbock, Texas, USA.

Lemaitre, C., de Langre, E., Hémon, P., 2010. Rainwater rivulets running on a stay cable subject to wind. European Journal of Mechanics - B/Fluids 29(4), 251–258.

Lemaitre, C., Hémon, P., de Langre, E., 2007. Thin water film around a cable subject to wind. Journal of Wind Engineering and Industrial Aerodynamics 95, 1259–1271.

Li, F.C., Chen, W.L., Li, H., Zhang, R., 2010a. An ultrasonic transmission thickness measurement system for study of water rivulets characteristics of stay cables suffering from wind–rain-induced vibration. Sensors and Actuators A 159, 12–23.

Li, H., Chen, W.L., Xu, F., Li, F.C., Ou, J.P., 2010b. A numerical and experimental hybrid approach for the investigation of aerodynamic forces on stay cables suffering from RWIV. Journal of Fluids and Structures 26, 1195–1215.

Li, Y.L., Lu, W., Tao, Q.Y., Xiong, W.B., 2007. Study on rain-wind induced vibration of cables in cable-stayed bridges by wind tunnel test. Journal of Experiments in Fluid Mechanics 21, 36–44. (in Chinese)

Li, Y.L., Jing, H.Q., Xia, Y., Xu, Y.L., Xiang, H.Y., 2015. Measurement of rivulet movement on inclined cables during rain–wind induced vibration. Sensors and Actuators A 230, 17–24.

Macdonald, J.H.G., Larose, G.L., 2006. A unified approach to aerodynamic damping and drag/lift instabilities, and its application to dry inclined cable galloping. Journal of Fluids and Structures 22, 229–252.

Mahbub Alam, MD., Zhou, Y., 2007. Turbulent wake of an inclined cylinder with water running. Journal of Fluid Mechanics 589, 261–303.

Main, J.A., Jones, N.P., 1999. Full-scale measurements of stay cable vibration, Wind Engineering into the 21st Century, A. A. Balkema, Rotterdam, 963–970.

Matsumoto, M., Saitoh, T., Kitazawa, M., Shirato, H., Nishizaki, T., 1995. Response characteristics of rain–wind Induced vibrations of stay-cables of cable-stayed bridges. Journal of Wind Engineering and Industrial Aerodynamics 57, 323–333.

Matsumoto, M., Shiraishi, N., Shirato, H., 1992. Rain–wind induced vibration of cables of cable-stayed bridges. Journal of Wind Engineering and Industrial Aerodynamics 43, 2011–2022.

Matsumoto, M., Yagi, T., Goto, M., Sakai, S., 2003. Rain–wind-induced vibration of inclined cables at limited high reduced wind velocity region. Journal of Wind Engineering and Industrial Aerodynamics 91, 1–12.

Matsumoto, M., Yagi, T., Sakai, S., Ohga, J., Okada, T., 2005. Steady wind force coefficients of inclined stay cables with water rivulet and their application to aerodynamics. Wind and Structures 8, 107–120.

Ni, Y.Q., Wang, X.Y., Chen, Z.Q., Ko, J.M., 2007. Field observations of rain–wind induced cable vibration in cable-stayed Dongting Lake Bridge. Journal of Wind Engineering and Industrial Aerodynamics 95, 303–328.

Nikitas, N., Macdonald, J.H.G., 2015. Aerodynamic forcing characteristics of dry cable galloping at critical Reynolds numbers. European Journal of Mechanics - B/Fluids 49, 243–249.

Nikitas, N., Macdonald, J.H.G., Andersen, T.L., 2012. Critical Reynolds number and galloping instabilities: experiments on circular cylinder. Experiments in Fluids 52, 1295–1306.

Panton, R.L., 2013. Incompressible Flow, Fourth Edition, John Wiley & Sons, Inc., Hoboken, New Jersey, USA.

Robertson, A.C., Taylor, I.J., Wilson, S.K., Duffy, B.R., Sullivan, J.M., 2010. Numerical simulation of rivulet evolution on a horizontal cable subject to an external aerodynamic field. Journal of Fluids and Structures 26, 50–73.

Seidel, C., Dinkler, D., 2006. Rain–wind induced vibrations-phenomenology, mechanical modeling and numerical analysis. Computers & Structures 84, 1584–1595.

Taylor, I.J., Robertson, A.C., 2011. Numerical simulation of the airflow-rivulet interaction associated with the rain–wind induced vibration phenomenon. Journal of Wind Engineering and Industrial Aerodynamics 931–944.

Wilde, K., Witkowski, W., 2003. Simple model of rain–wind-induced vibrations of stayed cables. Journal of Wind Engineering and Industrial Aerodynamics 91, 873–891

Xia, Y., Fujino, Y., 2006. Auto-parametric vibration of a cable-stayed-beam structure under random excitation. Journal of Engineering Mechanics 132, 279–286.

Xu, Y.L., Li, Y.L., Shum, K.M., Kwok, K.C.F., Kwok, K.C.S., Hitchcock, P.A., 2006. Aerodynamic coefficients of inclined circular cylinders with artificial rivulet in smooth flow. Advances in Structural Engineering 9, 265–278.

Xu, Y.L., Wang, L.Y., 2003. Analytical study of wind–rain-induced cable vibration: SDOF model. Journal of Wind Engineering and Industrial Aerodynamics 91, 27–40.

Zdravkovich, M.M., 1997. Flow around circular cylinders, 1. Fundamentals, Oxford University Press, Oxford, UK.

Zhan, S., Xu, Y.L., Zhou, H.J., Shum, K.M., 2008. Experimental study of wind–rain-induced cable vibration using a new model setup scheme. Journal of Wind Engineering and Industrial Aerodynamics 96, 2438–2451.

Zuo, D., Jones, N.P., 2010. Interpretation of field observations of wind- and rain–wind induced stay cable vibrations. Journal of Wind Engineering and Industrial Aerodynamics 98, 73–87.

Zuo, D.L., Jones, N.P., Main, J.A., 2008. Field observation of vortex- and rain–wind induced stay-cable vibrations in a three-dimensional environment. Journal of Wind Engineering and Industrial Aerodynamics 96, 1124–1133.